Estimation of Rain Rate from Airborne Doppler W-Band Radar in CalWater-2

C. W. FAIRALL

NOAA/Earth System Research Laboratory, Physical Sciences Division, Boulder, Colorado

SERGEY Y. MATROSOV AND CHRISTOPHER R. WILLIAMS

Cooperative Institute for Research in Environmental Sciences, University of Colorado Boulder, and NOAA/Earth System Research Laboratory, Physical Sciences Division, Boulder, Colorado

E. J. WALSH

NOAA/Earth System Research Laboratory, Physical Sciences Division, Boulder, Colorado

(Manuscript received 9 February 2017, in final form 20 November 2017)

ABSTRACT

The NOAA W-band radar was deployed on a P-3 aircraft during a study of storm fronts off the U.S. West Coast in 2015 in the second CalWater (CalWater-2) field program. This paper presents an analysis of measured equivalent radar reflectivity factor Z_{em} profiles to estimate the path-averaged precipitation rate and profiles of precipitation microphysics. Several approaches are explored using information derived from attenuation of Z_{em} as a result of absorption and scattering by raindrops. The first approach uses the observed decrease of Z_{em} with range below the aircraft to estimate column mean precipitation rates. A hybrid approach that combines Z_{em} in light rain and attenuation in stronger rain performed best. The second approach estimates path-integrated attenuation (PIA) via the difference in measured and calculated normalized radar cross sections ($NRCS_m$ and $NRCS_c$, respectively) retrieved from the ocean surface. The retrieved rain rates are compared to estimates from two other systems on the P-3: a Stepped Frequency Microwave Radiometer (SFMR) and a Wide-Swath Radar Altimeter (WSRA). The W-band radar gives reasonable values for rain rates in the range 0–10 mm h^{-1} with an uncertainty on the order of 1 mm h^{-1}. Mean profiles of Z_{em}, raindrop Doppler velocity, attenuation, and precipitation rate in bins of rain rate are also computed. A method for correcting measured profiles of Z_{em} for attenuation to estimate profiles of nonattenuated profiles of Z_e is examined. Good results are obtained by referencing the surface boundary condition to the NRCS values of PIA. Limitations of the methods are discussed.

1. Introduction

Precipitation is one of the most difficult and confounding meteorological variables to measure accurately and to sample sufficiently for meaningful averages. Most applications (e.g., hydrology, oceanic salinity budgets, global energy balances, soil moisture analysis) require grid-averaged precipitation rates. Because of the greatly patchy nature of precipitation, undersampling makes the use of surface-based conventional rain gauges problematic.

Ground-based scanning radars and satelliteborne radars can greatly improve sampling, but they introduce a host of accuracy issues (e.g., Lee and Zawadzki 2006; Haynes et al. 2009). Two common issues with radar-based methods are the absolute calibration of the radar and the variation of radar–rain retrieval relationships with precipitation microphysics (Steiner et al. 2004; Lee and Zawadzki 2006). Conventional rain gauges have biases associated with wind effects on collection efficiency that are geometry dependent (Ciach 2003); gauges typically provide accumulations, and estimates of rain rate from gauge data often have poor time resolution. Disdrometers, which measure the raindrop size distribution (DSD), offer a superior surface characterization of precipitation microphysics because both the rain rate R and the equivalent radar reflectivity factor Z_e can be computed from the observations.

ⓐ Denotes content that is immediately available upon publication as open access.

Corresponding author: C.W. Fairall, chris.fairall@noaa.gov

While precipitation reaching the surface is the over-arching variable in many weather applications, precipitation formation processes are a critical research topic. Observational research into cloud–precipitation microphysical relationships has been dominated by airborne in situ DSD and ground-based millimeter-wavelength Doppler radar–observing systems (Kollias et al. 2007). The advent of DSD and Doppler spectrum moment techniques (Frisch et al. 1995, 1998) increased the utility of remote sensing methods, which have subsequently expanded to a variety of approaches [including multiwavelength, multi-Doppler peak, clear-air vs drop scattering modes; for more information see Tridon et al. (2013), Tridon and Battaglia (2015), and Williams (2016)]. Airborne (Galloway et al. 1999) and satelliteborne (Haynes et al. 2009) millimeter-wavelength radars have greatly expanded the scope of radars to investigate the spatial distribution and vertical structure of precipitating cloud systems. Multiwavelength methods have a rich history of application with surface-based systems (Firda et al. 1999; Williams 2012), but applications with airborne systems (e.g., Tian et al. 2007) are relatively rare—principally because of engineering constraints associated with matching beamwidth and performance characteristics at different wavelengths when space and weight conflict with aerodynamic performance. Millimeter-wavelength radars have the major advantage that they are sensitive to both clouds and precipitation and, because of their smaller size, are ideal for airborne platforms. The advantages of multiple wavelength techniques are moot if you have only one radar (e.g., TRMM, https://trmm.gsfc.nasa.gov/overview_dir/pr.html; and CloudSat, http://cloudsat.atmos.colostate.edu/instrument). Thus, we are motivated to squeeze as much information as we can from a single wavelength system.

One important weakness of moment-based methods in estimating precipitation rate and microphysics is that the zeroth, first, and second moments of the radar-reflectivity-weighted Doppler velocity spectrum are essentially the sixth–eighth moments of the DSD for the Rayleigh-type scattering [see (9) in Frisch et al. 1995]. Thus, radar moment methods may poorly constrain rain-rate retrieval, which is essentially the 3.67th moment of the DSD. An independent constraint of one or more of the lower-order DSD moments could improve radar rain-rate retrievals. In this paper we use radar attenuation as a constraint to estimate mean multiparameter profiles and time series of layer-averaged rain rates below an airborne W-band Doppler radar. The observations we are using are from the NOAA Physical Science Division (PSD) W-band radar (Moran et al. 2012) deployed on a NOAA P-3 aircraft for seven flights during the second CalWater (CalWater-2; CalWater-2015) field program off the U.S. West Coast in 2015 (Ralph et al. 2016).

This paper presents an analysis of processing measured equivalent radar reflectivity factor profiles Z_{em} to estimate precipitation rate using the observed decrease of Z_{em} with range below the aircraft. The rain rate is approximately proportional to the attenuation coefficient in rain (i.e., the slope of the reflectivity profile, assuming a prevalence of rain attenuation over changes of nonattenuated reflectivity Z_e) as described in Matrosov (2007). We find that the two-tiered rain-rate retrieval method of Chandra et al. (2015), where large rain rates are computed from the attenuation of uncalibrated Z_{em} and light rain rates (less than approximately $1 \, \text{mm h}^{-1}$) are estimated from calibrated reflectivity using a Z_e–R parameterization, is an effective procedure. The Chandra et al. (2015) two-tiered methodology was based on ground-based vertically pointing Ka-band radar observations where attenuation estimates fell below measurement uncertainties for light rain rates.

A second but related method to estimate rain rate uses the measured normalized radar cross section NRCS_m retrieved from the return of the ocean surface. Since NRCS is fairly well characterized as a function of wind speed and angle relative to nadir (Li et al. 2005), the calculated normalized radar cross section NRCS_c is independent of radar attenuation. Thus, the difference between the measured and calculated NRCS represents the total column attenuation, which is also known as the path-integrated attenuation (PIA). As with the reflectivity gradient rain-rate method, the estimated PIA is related to rain rate such that PIA yields an estimate of the total column average rain rate below the aircraft (Meneghini et al. 1983). The total rain-rate estimates retrieved from the W-band radar measurements are compared to estimates from two other systems on the P-3: a Stepped Frequency Microwave Radiometer (SFMR; Uhlhorn et al. 2007) and a Wide-Swath Radar Altimeter (WSRA; Walsh et al. 2014).

In addition to estimating the layer-averaged rain rate, we wish to investigate the use of profiles of radar-derived parameters to retrieve information about precipitation microphysics. Here we explore the value added by attenuation observations. The approach centers on averages of radar profiles of the first three spectral moments plus attenuation in bins of rain rate. We have applied the Hitschfeld–Bordan inversion technique of Iguchi and Meneghini (1994) to retrieve profiles of unattenuated reflectivity using the surface return (NRCS) as the reference. This yielded profiles of Z_e consistent with values extrapolated to the aircraft altitude. Note that the surface reference (i.e., NRCS) and reflectivity gradient approaches have been used with the spaceborne W-band radar aboard CloudSat (e.g., Haynes et al. 2009; Matrosov 2011).

It is not practical to install an expensive radar on an aircraft just to measure rain rate. Our purpose here is to

evaluate the use of attenuation to improve information extraction from a millimeter-wavelength radar being used for cloud/precipitation research. Some caveats to consider: If rain rate is derived from the vertical gradient of measured reflectivity, then inhomogeneity in the vertical distribution of raindrops and cloud absorption will compromise the results. For rain rate derived from NRCS, uncertainty in the NRCS model and the 10-m wind speed retrieval are likely the largest source of error. Corrections for atmospheric gaseous absorption affect both approaches, but the errors are small if temperature/humidity profiles are available. The correction of measured reflectivity profiles relies on accurate NRCS measurement, the determination of the clear-air NRCS, and a specification of the attenuation-to-reflectivity relationship (which is somewhat sensitive to precipitation microphysics). NRCS can be used to provide an absolute calibration check of the radar reflectivity.

This paper is organized as follows: experimental details are given in section 2, radar–precipitation relationships are discussed in section 3; processing methods and analysis results are described in section 4, and section 5 has discussion and conclusions.

2. Experimental details

a. CalWater-2

The CalWater-2015 (Ralph et al. 2016) field deployment off the U.S. West Coast included NOAA's flagship Research Vessel *Ronald H. Brown* (*RHB*), as well as a P-3 and G-IV aircraft. The U.S. DOE–sponsored Atmospheric Radiation Measurement (ARM) Cloud Aerosol Precipitation Experiment (ACAPEX) campaign provided the DOE ARM Mobile Facility 2 (AMF2) observing system, mounted on the NOAA vessel, as well as the DOE G-1 aircraft and support for aerosol and microphysics sensors at the coast. The NASA ER-2 aircraft flew several missions as well with remote sensors tailored partly for validation of a prototype space-based sensor being tested on the International Space Station. The California Department of Water Resources (DWR)-sponsored statewide extreme precipitation network, tailored to observe landfalling atmospheric rivers (Ralph et al. 2016), was a foundation of the experiment. The observation period was January through March 2015. Here we discuss measurements taken on the NOAA P-3 aircraft.

b. P-3 measurements

NOAA's P-3 aircraft are equipped with a unique array of scientific instrumentation, radars, and recording systems for both in situ and remote sensing measurements of the atmosphere, Earth, and its environment (http://www.omao.noaa.gov/learn/aircraft-operations/aircraft/lockheed-wp-3d-orion). In situ sensors provided flight-level meteorological

and navigation information. The P-3 also deployed 80 Vaisala RD-94 dropsondes during the period in the region near 37°N, 127°W.

Rain-rate values were estimated from two systems on the P-3: the SFMR and the WSRA. These estimate rain rate averaged over altitude below the aircraft. The WSRA has 80 narrow beams spread over ±30° in the cross-track direction. It uses a subset of ±14° to estimate the sea surface mean square slope (mss) and the path-integrated attenuation at its Ku-band 16-GHz operating frequency. The nadir returned power is normalized to a constant mss and altitude. The maximum normalized returned power over a significant time interval is assumed to be rain free, and any decrease from that value is attributed to rain attenuation. Because the WSRA determines NRCS and mss independently by scanning incidence angles, it yields a fundamentally more unbiased measurement of the rain rate. It is also weakly attenuated compared to the W band, which reduces the resolution but allows for useful observations from greater altitudes and larger rain rates. Walsh et al. (2014) discuss the algorithm in detail and compare the results with the SFMR on the same aircraft and the National Mosaic and Multi-Sensor Quantitative Precipitation Estimation (QPE) system (Zhang et al. 2011; Lakshmanan et al. 2006) archive product from the NEXRAD network measurements. The SFMR passive technique for extracting the rain rate from its six C-band frequencies (4.74, 5.31, 5.57, 6.02, 6.69, 7.09 GHz) is more complex and has long been under development on NOAA aircraft (Black and Swift 1984; Uhlhorn et al. 2007; Walsh et al. 2014). Klotz and Uhlhorn (2014) detail the evolution of the technique and its present status, which produced the results compared with the W-band rain rates in this paper.

The observations we are focusing on are from the NOAA PSD W-band radar deployed on the P-3 for seven flights between 27 January and 9 February 2015[1]. The radar is described in depth by Moran et al. (2012). The initial deployments were ship based (Moran et al. 2012; Ghate et al. 2014) but aircraft deployments began in 2013 (Fairall et al. 2014).

---

[1] Aircraft deployments include Tropical Storm Karen, Hurricane Patricia, and CalWater-2. Raw and processed data for the PSD observations can be found online (at ftp://ftp1.esrl.noaa.gov/psd3/cruises/CALWATER_2015/). Dropsonde profiles as Matlab.mat files from the G-IV are available (ftp://ftp1.esrl.noaa.gov/psd3/cruises/CALWATER_2015/G4/data/) as are the W-band radar data [ftp://ftp1.esrl.noaa.gov/psd3/cruises/CALWATER_2015/P3/Wband/; with the moment files in netCDF format in the *mom* directory, and the P-3 navigation and flight-level data in .txt files (which includes the SFMR) are in the *Aircraft* directory].

c. Radar configuration and calibration

The W-band radar operated in one Doppler spectra mode with a focus on measuring rain below the aircraft. Doppler spectra were recorded to disk every 0.3 s, and the first three moments (i.e., zeroth, first, and second) were calculated to estimate reflectivity, mean Doppler velocity, and Doppler velocity spectrum width. Pertinent radar operating parameters are listed in Table 1. Note that the first range gate was set to 489 m below the aircraft to avoid destroying the receiver from strong surface returns when the aircraft was below 500-m altitude.

For distributed targets within a radar resolution volume, the measured raw reflectivity factor $Z_{em\_raw}(h)$ ($mm^6 m^{-3}$) at range h (km) is related to the received power $P_r(h)$ via

$$Z_{em\_raw}(h) = C_{radar} \frac{\lambda^4}{\pi^5 |K|^2} P_r(h) h^2, \qquad (1)$$

where $|K|^2 = 0.82$ is a function of the complex refractive index of water at the radar operating wavelength $\lambda = 3.17$ mm, and C_{radar} is the radar calibration constant that incorporates all radar internal gains and losses plus other corrections discussed below. After calibrating the PSD W-band radar antenna at an antenna range, absolute reflectivity accuracy is expected to be approximately ± 1 dB. In C_{radar} we include a correction factor that accounts for the additional loss of 1.6 dB from the radome in the belly of the aircraft plus a correction determined by calibration against NRCS in clear conditions. The NRCS calibration flight was done on 9 February 2015, which was dominated by clear skies. The P-3 dropped 17 sondes; the mean 10-m wind speed was $4.7 \, m \, s^{-1}$ with a standard deviation of $0.5 \, m \, s^{-1}$. We determined a final correction to the radar constant, equivalent to $+0.2 \pm 1.0$ dB, to force observed NRCS to agree with values in Li et al. (2005) at an incidence angle of 12° (at this angle NRCS has minimal wind speed dependence). The uncertainty in this correction is a combination of scatter in measured NRCS at 12° and variability of specified values in Li et al. (2005). An uncertainty of 1 dB translates to an uncertainty in NRCS-derived rain rate of about $0.32 \, mm \, h^{-1}$ (weakly wind speed dependent) for an aircraft altitude of 2.5 km.

Because of attenuation, Z_e is given as

$$Z_e(h) = Z_{em\_raw}(h)^* \exp\left[0.2 \ln(10) \int_0^h \gamma_{total}(s) \, ds\right], \qquad (2)$$

where γ_{total} is the total specific attenuation (dB km^{-1}) at range s (km) of length ds (km) and is composed of specific attenuation from oxygen γ_o, water vapor γ_{vapor},

TABLE 1. Specifications of the PSD W-band radar for CalWater-2 flights.

Parameter	Value
Radar operating frequency (GHz)	94.56
Radar operating wavelength (mm)	3.17
Number of range gates	150
Range resolution (m)	25
Distance to first range gate (m)	489
Distance to last range gate (m)	4214
Number of Doppler velocity bins	128
Doppler velocity bin resolution (m s^{-1})	0.12
Nyquist velocity (m s^{-1})	7.68
Number of spectral averages	9
Minimum detectable SNR (dB)	-20
Minimum detectable reflectivity at 1 km (dBZ)	-34
Dwell time per average spectrum (s)	0.3
Antenna diameter (m)	0.305
Antenna gain (dB)	46
Antenna beamwidth (°)	0.7

cloud γ_{cloud}, and precipitation γ_{rain}. The total specific attenuation can be expressed as

$$\gamma_{total}(s) = \gamma_o(s) + \gamma_{vapor}(s) + \gamma_{cloud}(s) + \gamma_{rain}(s). \qquad (3)$$

For the remainder of this paper we will use the notation that Z_{em} is defined as the raw reflectivity corrected by the combined absorption of water vapor and oxygen ($\gamma_v = \gamma_o + \gamma_{vapor}$),

$$dBZ_{em}(h) = dBZ_{em\_raw}(h) + G_v(h), \qquad (4)$$

where $dBZ_{em} = 10 \log_{10}(Z_{em})$ and G_v is the gaseous attenuation, which is defined as

$$G_v(h) = 2^* \int_0^h \gamma_v(s) \, ds. \qquad (5)$$

The factor of 2 in this equation arises because the radar has a two-way path. If we assume the cloud attenuation can be neglected, then changes in Z_{em} can be related to rain attenuation. A stratus cloud with a liquid water content of $0.1 \, g \, m^{-3}$ would have an attenuation of approximately $0.4 \, dB \, km^{-1}$—roughly comparable to rain with a rate of $0.5 \, mm \, h^{-1}$ (e.g., Matrosov 2009), representing a bias in rain-rate estimates based on attenuation.

Values of γ_v were obtained using the atmospheric absorption methods from the International Telecommunication Union (www.itu.int/dms_pubrec/itu-r/rec/p/R-REC-P.676-3-199708-S!!PDF-E.pdf). For CalWater-2 we computed $G_v = 2.2$ dB for $h = 2.5$ km using the mean water vapor, temperature, and pressure profiles from 19 CalWater-2 sondes dropped in the observation region by the

TABLE 2. Coefficients for rain-rate dependence of Z_e [(7)] and γ_{rain} [(8)] at W band. *Bootstrap* refers to a relationship based on NRCS rain rates and observed attenuation and reflectivity. Lhermitte and Kollias values are computed from Marshall–Palmer DSD. Matrosov (2007, 2010) values are computed from disdrometer DSD measurements. P-3 PIP calculations are from the airborne in situ DSD measurements on 6 Feb 2015. More recent direct estimates (bold values) are used to compute an average and uncertainty. Values in the table correspond to Z_e in mm^6 m^{-3}, γ in dB km^{-1}, and R in mm h^{-1}.

Source	a_z	b_z	a_γ	b_γ	α_γ	β_γ
Lhermitte (2002)	63	0.67	1.25	0.75	0.0121[a]	1.12[a]
Kollias et al. (2003)			0.89	0.83		
Matrosov (2007)			0.81	1.00		
Matrosov (2010)	**36**	**1.03**	1.13	0.89	0.051[a]	0.86[a]
Direct γ–Z_e fit					**0.033**	**0.97**
Linear γ–R fit	**(36)**	**(1.03)**	**0.9**	**1.00**	0.028[a]	0.97[a]
Bootstrap	**15**	**1.1**	**1.0**	**1.0**	0.085[a]	0.91[a]
Direct γ–Z_e fit (Fig. 10)					**0.05**	**1.0**
P-3 PIP	**23**	**0.94**	**0.70**	**1.00**	0.026[a]	1.06[a]
Direct γ–Z_e fit					**0.058**	**0.85**
Linear γ–Z_e fit					0.040	1.00
Average bold uncertainty	25 ± 7	1.02 ± 0.06	0.87 ± 0.09	1.0	0.047 ± 0.01	0.94 ± 0.06

[a] Implies γ–Z_e coefficients computed from the Z_e–R and γ–R relationships.

NOAA G-IV on 5 February 2015 (precipitable water path of 2.2 cm from the surface to and an aircraft altitude of 2.5 km). The term $G_v(h)$ was 0.07 dB at the first radar range gate and 2.20 dB at the surface. The variability (standard deviation associated with the variability of the sonde profiles) of $G_v(h)$ was ±0.18 dB at the surface and ±0.12 dB at 1-km altitude.

3. Radar–precipitation relationships

a. Processing for surface cross section

With regard to surface returns, at near-nadir incidence the W-band radar observes a strong spike in measured Z_{em} from the ocean surface (Li et al. 2006) that is referred to as the ocean scattering cross section $\sigma_0 = \eta_0 * \delta R$ (where δR is the radar range gate thickness). The measured reflectivity factor is converted to NRCS$_m$ using

$$\text{NRCS}_m = 10 * \log_{10}(\sigma_0) = 10 * \log_{10}\left[\frac{\pi^5 |K^2|}{\lambda^4} \delta R\right] + \text{dB} Z_{em} - 180, \quad (6)$$

where 180 is a conversion factor converting reflectivity factor from mm^6 m^{-3} to m^3. At W band and with 25-m range resolution, the first term on the right-hand side of (6) is 137.9.

b. Rain profile retrievals using reflectivity gradient

After correcting for attenuation, the simplest R (mm h^{-1}) retrievals are based on Z_e–R power-law relationships of the form

$$Z_e = a_Z R^{b_Z}. \quad (7)$$

The Z_e–R relationships are estimated in several ways, for example, fitting observed Z_e versus surface-based

rain measurements or using airborne or ground-based measurements of the rain DSD to compute nonattenuated values of Z_e and R. The rain rate can be expressed as a function of Z_e by inverting (7).

Note that (7) is poorly posed for retrieving rain rate at W band, partly because of attenuation and partly because Z_e at W band includes both the Rayleigh scattering regime for small raindrops and the non-Rayleigh scattering regime for raindrops greater than about 0.8 mm in diameter. Because of non-Rayleigh scattering, the changes in nonattenuated reflectivity at W band with increasing rain rate are not that pronounced as at lower frequencies.

The relationship between rain-specific attenuation and rain rate can be expressed with a power law of the form

$$\gamma_{rain} = a_\gamma R^{b_\gamma}. \quad (8)$$

Some estimated coefficients from previous studies are given in Table 2. Given the data scatter in the γ_{rain}–R correspondence, (8) can be assumed to be linear with $b_\gamma = 1$ (Matrosov 2007). The bootstrap values given in Table 2 are obtained from relationships based on NRCS rain rates and observed attenuation and reflectivity, that is, solely determined by CalWater-2 W-band observations. The CalWater P-3 values are computed from a Droplet Measurement Technologies Precipitation Imaging Probe (PIP), which sizes drops in 62 equally spaced bins from 0.10 to 6.2 mm in diameter. The Matrosov (2010), bootstrap, and P-3 PIP are considered the most representative for these observations, so they were used to compute the averages.

The linearized mean relationship between the attenuation coefficient γ_{rain} and rain rate is written as

$$R = c\gamma_{\text{rain}}\left[\frac{1.1}{\rho_a(z)^{0.45}}\right] = c\gamma_{\text{rain}}*k(z), \tag{9}$$

where $c = 1.11\,\text{km}\,\text{dB}^{-1}\,\text{mm}\,\text{h}^{-1}$ as estimated from T-matrix modeling using DSDs collected with the Joss–Waldvogel disdrometer during a Hydrometeorology Testbed (HMT) field project in California (Matrosov 2010). The term on the right, $k(z)$, is a dimensionless correction factor accounting for an increase in raindrop fall velocity as the air density ρ_a ($\text{kg}\,\text{m}^{-3}$) decreases with height z above the surface (Foote and duToit 1969). The factor 1.1 is $\rho_0^{0.45}$, where $\rho_0 = 1.25\,\text{kg}\,\text{m}^{-3}$ is the density of air at the surface. For this paper a fixed density correction of 1.04 was used, which corresponded to an altitude of 1.0 km and CalWater-2 atmospheric conditions.

Since attenuation coefficients are usually specified in decibels per kilometer, they can be related to the vertical gradient of measured $\text{dB}Z_{\text{em}}$ as

$$\frac{d(\text{dB}Z_{\text{em}})}{dz} = \frac{d(\text{dB}Z_e)}{dz} + 2\gamma_{\text{rain}}, \tag{10}$$

where the first term on the right-hand side describes changes of nonattenuated reflectivity $\text{dB}Z_e$, If the vertical gradient of $\text{dB}Z_e$ is small compared to that resulting from attenuation, then the rain attenuation can be computed from the slope of $\text{dB}Z_{\text{em}}$ versus altitude as follows:

$$\gamma_{\text{rain}} = 0.5\frac{d(\text{dB}Z_{\text{em}})}{dz}, \tag{11}$$

where each term in (11) is height dependent. Equation (11) provides the estimate of the mean attenuation coefficient under the assumption that the vertical changes of nonattenuated reflectivity are small compared to changes of observed reflectivity as a result of attenuation (i.e., the gradient of $\text{dB}Z_e$ is much smaller than the gradient of $\text{dB}Z_{\text{em}}$). This equation can be applied to different segments of the entire rain layer by calculating a mean gradient within the segments of the layer. Note also that the Doppler velocity threshold (Chandra et al. 2015) provides a way of choosing segments/layers where the gradient approach provides sensible results.

c. Path-integrated rain retrievals

The radar backscatter from the sea surface allows another method to compute the path-averaged rain rate from the total attenuation from the aircraft to the surface. For our purposes here we restrict the analysis to nadir-pointing profiles only, so at a given wavelength the NRCS_c is a function of wind speed only,

$$\text{NRCS}_c = |F(0)|^2 / \text{mss} = f(U_{10}), \tag{12}$$

where U_{10} is the wind speed at a height 10 m above the ocean, $F(0)^2 = 0.32$ is the Fresnel reflection coefficient at 20°C for seawater at W band at normal incidence and mss is the mean squared slope of the surface waves. Thus, the difference between the measured NRCS_m and the value, NRCS_c, gives a PIA defined as

$$\text{PIA}_R = \text{NCRS}_c - \text{NCRS}_m. \tag{13}$$

The NRCS-based rain rate, R_{nc}, can be computed as

$$R_{nc} = ck(z)\frac{\text{NRCS}_c - \text{NRCS}_m}{2h_s}, \tag{14}$$

where h_s is the range to the surface. The advantage of (14) is that it does not require near-uniform vertical profiles of rain but gives the mean rain rate between the aircraft and the surface. The disadvantage is that it requires a specification of NRCS_c; NRCS_m is computed from Z_{em} at the surface as per (6). The model for NRCS_c we are using is

$$\text{NRCS}_c = 14.1 - 0.2*U_{10} - 0.004*U_{10}^2, \tag{15}$$

which is based on fits to NRCS_m for clear-sky data in previous flights. The coefficients in (15) correspond to U_{10} ($\text{m}\,\text{s}^{-1}$) as obtained from the SFMR measurements. If (14) yields a negative number, then we set R_{nc} to zero.

d. Profiles of Z_e versus Z_{em}

A considerable amount of work in the literature concerns retrieving the true (i.e., nonattenuated) Z_e profile from the radar-observed profile. The simplest approach is to combine (10) with a specification of attenuation in terms of Z_e as in (8), where

$$\gamma_{\text{rain}} = \alpha_\gamma Z_e^{\beta_\gamma}. \tag{16}$$

In this case, Iguchi and Meneghini (1994) show that the Hitschfeld and Bordan (1954) relation can be expressed as

$$Z_e(h) = \frac{Z_{\text{em}}(h)}{[1 - qS(h)]^{1/\beta_\gamma}}, \tag{17}$$

where

$$S(h) = \int_0^h \alpha_\gamma Z_{\text{em}}^{\beta_\gamma}(s)\,ds \tag{18}$$

and

$$q = 0.2\beta_\gamma \ln(10). \tag{19}$$

Note that the integral $S(h)$ is in terms of Z_{em}, so the right-hand side of (17) is solely in terms of measured quantities.

The use of (17) is known to be problematical at W band because the absorption is large and the retrieval is referenced to the value of Z_{em} nearest to the aircraft. In our case, we must also extrapolate the Z_{em} profile from the first range gate (489 m below the aircraft) up to the aircraft to compute $S(h)$. For this paper, we have used $NRCS_m$ to reference the profile at the surface (Iguchi and Meneghini 1994),

$$Z_e(h) = \frac{Z_{em}(h)}{\{A_s^{\beta_\gamma} + q[S(h_s) - S(h)]\}^{1/\beta_\gamma}}, \qquad (20)$$

where $S(h_s)$ is the value of $S(h)$ at the surface and

$$A_s = 10^{(NRCS_m - NRCS_c)/10} = 10^{-PIA/10}. \qquad (21)$$

This approach has two advantages: the correction is most accurate where it is largest (near the surface) and it does not depend on the extrapolation of the Z_{em} profile above the first range gate. The second point follows because

$$S(h_s) - S(h) = \int_0^{h_s} \alpha_\gamma Z_{em}^{\beta_\gamma}(s)\, ds - \int_0^h \alpha_\gamma Z_{em}^{\beta_\gamma}(s)\, ds$$
$$= \int_h^{h_s} \alpha_\gamma Z_{em}^{\beta_\gamma}(s)\, ds, \qquad (22)$$

which depends only on the profile between h and the surface.

4. Processing and analysis

Only one flight (1900–2100 UTC 5 February 2015) yielded significant "stratiform" rain that is suitable for our analysis. Here we use the term *stratiform* to describe wide-scale, weakly convective precipitation associated with midlatitude frontal regions (referred to as atmospheric rivers). We are not using it to refer to broad areas of precipitation in outflow regions from deep tropical convection. The flight on 7 February 2015 had significant rainfall, which is suitable for applying the NRCS approach, but it is too patchy to be able to claim relative vertical homogeneity (i.e., the presence of uniform rain everywhere in a layer from the aircraft altitude to the surface). On 5 February 2015, the aircraft was flying below a large region of precipitating clouds (i.e., it was not in cloud). In some periods there were low-level "scud" clouds below the

aircraft with tops around 0.5 km. Radar measurements from the NOAA ship *Ronald H. Brown* indicated cloud tops at 7-km altitude with a freezing-level bright band at about 3-km altitude. Photographs taken from the P-3 and a visible satellite image can be found online (ftp://ftp1.esrl.noaa.gov/psd3/cruises/CALWATER_ 2015/P3/P3_02_05_2015/Pics_Plans_PPTs/Photos/).

An example of radar Z_{em} profile measurements is shown in Fig. 1. The P-3 location during the flight is shown in Fig. 2 with color-coded indications of 10-m wind speed from the SFMR. Measured and parameterized values of NRCS are shown in Fig. 3a with resultant rain rate in Fig. 3b. In Fig. 4 we show rain-rate estimates (smoothed to a 1-min time resolution) from NRCS, the SFMR, and the WSRA for the entire 3-h period. The WSRA has been biased corrected for slow variations in the transmit power. Some elements of the phased array antenna were not operating correctly and the problem was intermittent. The comparison between NRCS and SFMR retrievals is better but still not good for lighter rain rates. The agreement is better at rain rates greater than about $2\,\mathrm{mm\,h^{-1}}$. The correlation coefficient between NRCS and SFMR rain rates is 0.81, while for NRCS–WSRA rain rates it is 0.71.

The peak NRCS rain rate in Fig. 4 is about $10\,\mathrm{mm\,h^{-1}}$, which is the approximate limit of the radar when flying at 2.5 km with $20\,\mathrm{m\,s^{-1}}$ 10-m wind speed. This is because surface returns are no longer detectable for greater rain rates (e.g., a gap in the surface returns at 1920 UTC in Fig. 1).

a. Processing methods

We have examined several methods for estimating the rain rate from the measured reflectivity profiles from two points of view: 1) time series of layer-averaged rain rate computed from each profile of Z_{em} and 2) profiles of radar variables averaged in bins of rain rate. The time series methods are as follows:

1) Compute a linear regression for each observation of dBZ_e versus h of the form $dBZ_{em} = dBZ_{ei} + slope*h$. The rain rate is then estimated from this slope using (9). The intercept, dBZ_{ei}, is reflectivity at the aircraft height ($h = 0$), which is an estimate of the unattenuated dBZ_e (valid when rain is observed in the first range gate and assumes that rain is present in the whole layer from the aircraft altitude to the surface).

2) Compute a layer-averaged attenuation from the difference in reflectivity at two range gates as $(dBZ_{em1} - dBZ_{em2})/(h1 - h2)$ and get an estimate of rain rate using (9). This estimate is somewhat akin to the NRCS estimate but does not depend on a surface
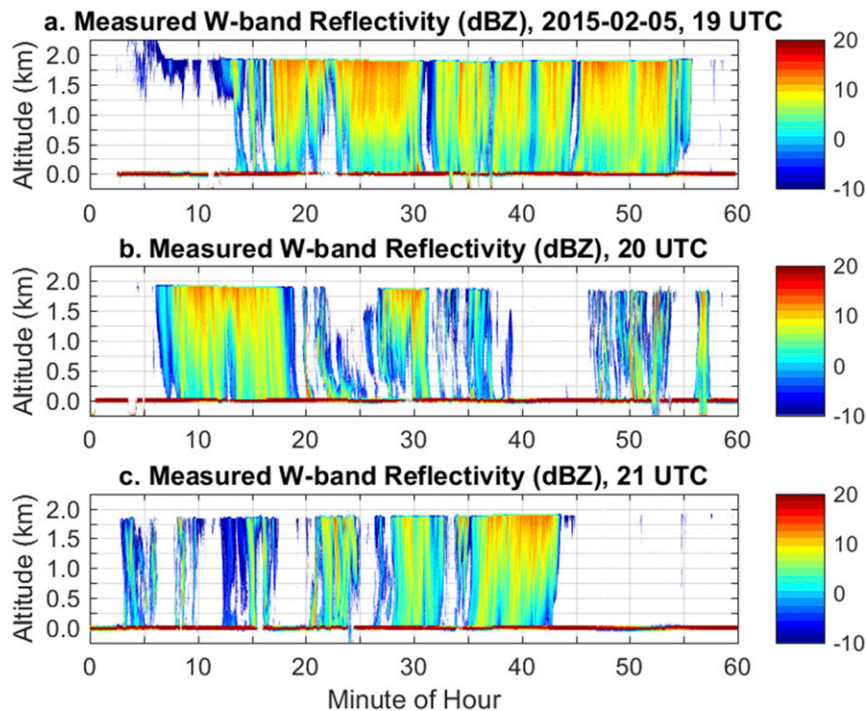
FIG. 1. Time–range cross section of reflectivity (dBZ_{em}) for (a) 1900, (b) 2000, and (c) 2100 UTC 5 Feb 2015. Vertical ordinate is height above the surface (altitude); horizontal ordinate is minutes for each hour (UTC). Surface return is apparent (bright red line at altitude near 0). Aircraft descended from 5 to 2.5 km in the beginning of the record. Banking maneuvers are visible as the short periods of extended range in the surface return (e.g., 20 h, 53 min). Note the period just after 19 h, 20 min when attenuation is so great there is no surface return.

backscatter model. Here we have used range gates at altitudes of $h_1 = 0.67$ km (altitude = 1.83 km) and $h_2 = 2.3$ km (altitude = 0.20 km).

3) We have also used a hybrid approach following Chandra et al. (2015) where Z–R and attenuation retrievals are combined. The procedure is to
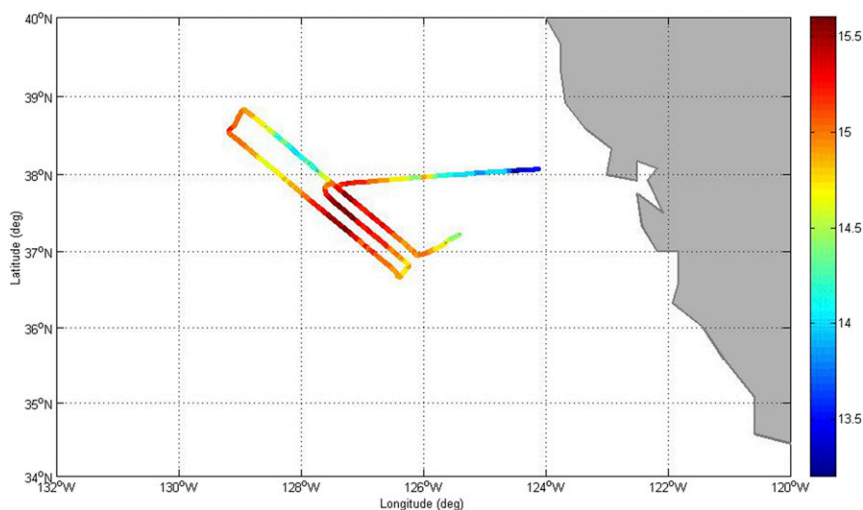
FIG. 2. Flight path of the NOAA P-3 for 1900–2200 UTC 5 Feb 2015. Color of the path denotes 10-m wind speed (m s^{-1}) from the SFMR. Satellite image for this day can be found online (ftp://ftp1.esrl.noaa.gov/psd3/cruises/CALWATER_2015/P3/P3_02_05_2015/Pics_Plans_PPTs/Photos/SatelliteImage_05Feb2015.png).
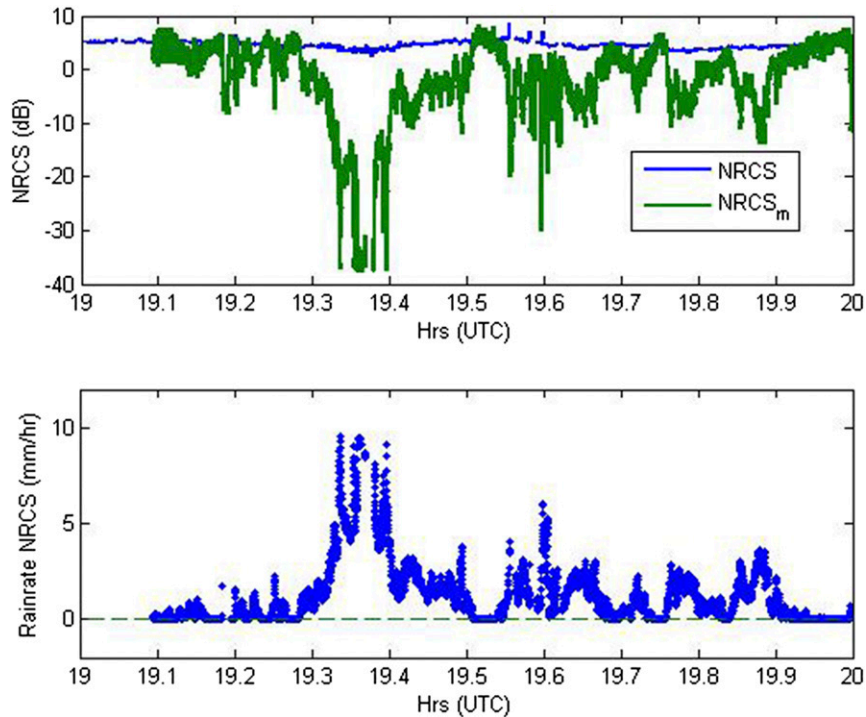
FIG. 3. (top) Sample time series of modeled NRCS$_c$ (blue) and NRCS$_m$ measured including attenuation (green) from 1900 UTC 5 Feb 2015 in CalWater-2. Note a few missing values just after 1935 UTC, when rain attenuation was sufficient to eliminate the surface return (you can see this as a notch in dBZ_{em} in Fig. 1 where the surface return disappears). At the end of the record there is no precipitation, so the blue and green lines coincide. (bottom) Precipitation from NRCS$_c$–NRCS$_m$.

compute an estimate of R from reflectivity at a selected range gate, Z_{em3}, via (7). If the measured Doppler velocity at h_3 is less than a threshold, then it replaces R with the value from method 2 (above). Here we used $h_3 = 0.67$ km and a Doppler velocity threshold of -3.0 m s^{-1}. Chandra et al. (2015) used a Doppler threshold of -5 m s^{-1} for a Ka-band radar. In the same conditions, a Doppler velocity observed at W band is about -3.5 m s^{-1} (see Firda et al. 1999 or Fig. 5 in Tian et al. 2007). Tridon and Battaglia (2015) note that the reflectivity departs significantly from the Rayleigh limit at fall velocities of 3.3 and 4.9 m s^{-1} for W and Ka bands, respectively. The slightly more conservative threshold $(-3.0$ m s$^{-1})$ we used reflects the stronger absorption at W band.

The bin-averaged methods use the rain rate from NRCS. We average the first three spectral moments and $d(\mathrm{dB}Z_e)/dh$ in bins of rain rate at every range gate. The mean attenuation profile for each rain-rate bin is $-0.5* < d(<\mathrm{dB}Z_{em}>)/dh>$, where $dh = 0.025$ km. Thus, we obtain profiles of mean Z_{em}, Doppler velocity, and attenuation at different rain rates.

b. Rain-rate time series

An important issue to solve is how to treat the non-ideal nature of the nonattenuated reflectivity profiles in the processing (Matrosov 2009). Examples of three types of dBZ_e profiles are shown in Fig. 5. A glance at Fig. 1 shows periods when there is no rain at aircraft
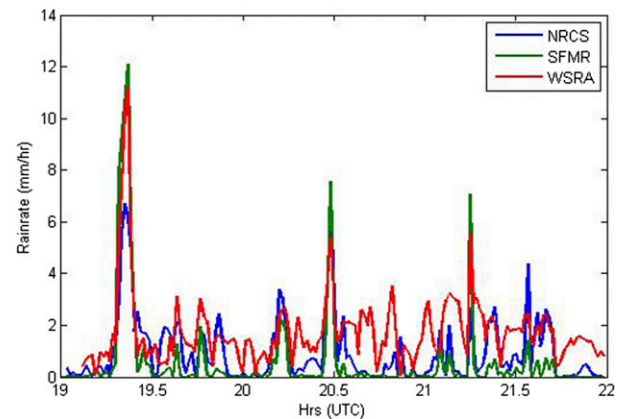
FIG. 4. As in Fig. 3, except that a 1-min smoothed form of the rain rate is shown for the entire period 1900 through 2200 for NRCS (blue), SFMR (green), and WSRA (red).
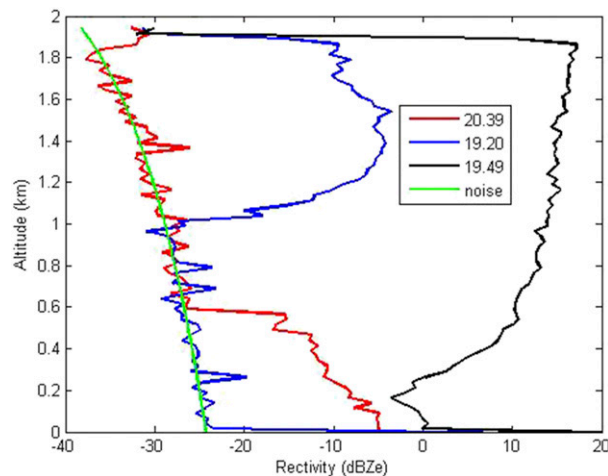
FIG. 5. Sample observed reflectivity profiles from 5 Feb 2015. Noise level of the radar (green line; in dBZ_{em} terms it increases with range from the radar). In the middle of the record with light precipitation from the surface up to 0.6 km (red line). Early in the record with no precipitation below 1 km (blue line). Later still with precipitation all the way to the surface (black line). The legend shows the time within the hour.

flight level or the first observable range gate (e.g., the period 2021–2026 UTC). Thus, a vertical derivative will indicate negative attenuation near the first range that has precipitation (see the red profile in Fig. 5). The blue line in Fig. 5 shows a profile where only rain occupies the region above 1 km. The black line in Fig. 5 shows a case with significant return throughout the profile.

We have examined rain-rate estimates using methods 1 and 2 smoothed to a 1-min time resolution. These are pure rain dBZ_e gradient–based approaches. Both methods can produce negative rain rates and substantial over-estimates of the rain rate when the precipitation below the aircraft is vertically inhomogeneous (i.e., rain is not present everywhere below the aircraft). One simple check to avoid the worse cases is to require the gradient be positive or to require that the dBZ_{em} at the first us-able range gate has measurable rain and that the dBZ_{em} at that range gate exceeds the value of dBZ_{em} near the surface. For values that do not meet the criteria, we set

the rain rate $= 0$. We found that method 3 (hybrid) is superior to methods 1 and 2, yielding a more accurate mean and higher correlation with R_{nc} (see Table 3). Figure 6 shows the rain-rate time series with method 3 and the NRCS-based method.

c. Bin-averaged profiles

Figure 7 shows profiles of mean dBZ_{em} and vertical Doppler velocity W averaged in bins of rain rate as determined by the NRCS method for the 3-h period on 5 February 2015. For each rain-rate interval, the means were computed for profiles where SNR > -10 dB, which is the minimum value yielding reliable estimates of Doppler velocity. The six rain-rate intervals used in the remainder of this paper are [0–0.25, 0.25–0.7, 0.7–1.5, 1.5–3, 3–6, and 6–13] mm h^{-1}. The average rain rates for each interval are listed in the legend of Fig. 7. The fraction of profiles that exceed the SNR minimum f_q is given in Table 4. The SFMR- and WSRA-based rain rates were too noisy and uncertain to use as an index for bin averaging. The measured Doppler vertical velocity is corrected for the pitch component of aircraft motion relative to the air via

$$W_c = W_m + \sin(\text{pitch})[-SOG*\cos(\psi - COG)$$
$$+ U_w*\cos(\psi - \text{Dir})]. \qquad (23)$$

The residual given by (23) should be the mean Doppler velocity of the precipitation. Here SOG is the aircraft speed over ground (between 100 and 140 m s^{-1}); COG is the aircraft course over ground, pitch is the aircraft pitch angle; ψ is aircraft heading; U_w and Dir are the wind speed (taken from the SFMR) and wind direction (taken from the P-3 flight-level data), respectively. Equation (23) is derived from the corrections in Fairall et al. (2014) when aircraft roll $= 0$ [equivalent to (7) in Heymsfield 1989]. A 1° pitch on the P-3 will change the observed Doppler velocity about 2 m s^{-1}, so the accuracy of the navigation system and the relative alignment of the radar are important. To evaluate this we compared the mean Doppler shift of the *surface* return with the correction using (23) as a function of pitch for the

TABLE 3. Comparison of mean rain rate (mm h^{-1}) and correlation coefficients for the different methods using the 1-min time series. The mean while raining is computed by selecting periods where $R_{nc} > 1$ mm h^{-1}. Rain2 refers to the mean of WSRA and SFMR rain rates.

Method	NRCS	Method 1 slope	Method 2 ΔZ_{em}	Method 3 hybrid	WSRA	SFMR
Mean rain rate (mm h^{-1})	1.13	1.3	1.3	0.93	1.7	0.6
Std dev rain rate (mm h^{-1})	1.25	2.25	2.13	2.0	1.43	1.75
Mean while raining (mm h^{-1})	2.1	2.4	2.8	2.4	2.0	1.4
Correlation with NRCS	1.0	0.65	0.70	0.79	0.71	0.81
Correlation with Rain2	0.79	0.54	0.58	0.72	0.96	0.97
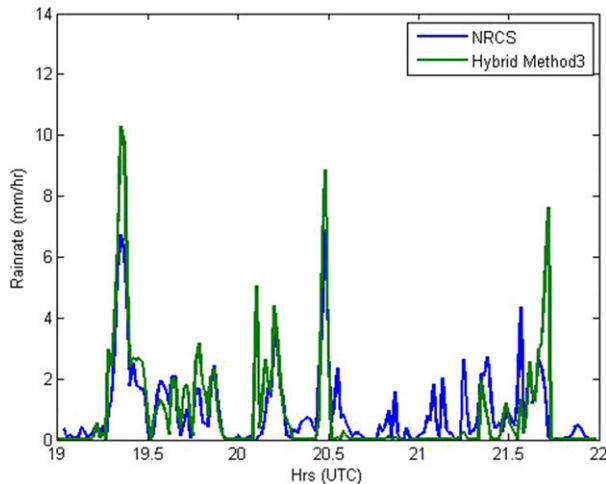
FIG. 6. Layer mean radar-derived rain-rate estimates from 5 Feb 2015. NRCS values (blue) are compared to the hybrid estimate (method 3) where $R = R_{\text{method2}}$ for $W_c < -3.0 \, \text{m s}^{-1}$ and $R = (Z_{\text{em}}/15)^{0.91}$ for $W_c > -3.0 \, \text{m s}^{-1}$. For method 2 the difference in reflectivity is computed between the two range gates at 1.83- and 0.20-km altitude; Z_{em} and W_c are taken from the range gate at 1.83-km altitude.

calibration flight on 9 February 2015. Since the aircraft is flying multiple headings, we can assume the mean Doppler velocity as a result of the surface current is 0 [see Haimov and Rodi (2013) for a more sophisticated example applied over land]. We applied a 0.5° correction to the P-3 pitch data to get zero mean Doppler at a pitch angle of 0. In the past (Fairall et al. 2014) we have done a similar pitch calibration using Doppler measurements from nonprecipitating clouds (which have negligible sedimentation velocity) in the first range gates below the aircraft. However, in CalWater-2 we did not have sufficient periods of nonprecipitation clouds just below the aircraft.

The following are some factors to note in Fig. 7:

1) The mean reflectivity value near the surface for the maximum rain rate is $-16 \, \text{dB}Z$, which is greater than, but close to, the radar noise level ($-24 \, \text{dB}Z$; see Fig. 5).

2) The slopes at lower rain rates are confined to the upper part of the profile and are actually larger than the slopes for intermediate rain rates. This likely indicates inhomogeneous profiles with most of the rain confined within 1 km below the aircraft. Thus, attenuation deduced from this regime is not reliable (i.e., gradients of nonattenuated reflectivities are not small compared to the gradients resulting from attenuation).

3) The $\text{dB}Z_{\text{em}}$ values at the top of the measured profiles for the two largest rain-rate bins are about the same. The slope for the highest rain rate shows much more attenuation, so a lot of the signal has been

lost between the aircraft and the first range gate (about 10 dB).

4) Mean Doppler velocities are between -3 and $-4.5 \, \text{m s}^{-1}$ and roughly become more negative with increasing rain rate. Doppler velocity is not the same as drop sedimentation velocity. The W-band radar is less sensitive (relative to the Rayleigh scattering regime) to droplets larger than about 1 mm. Thus, smaller drops with lower fall velocities are more heavily weighted than for radars at longer wavelengths. A Doppler velocity of $[-3.0 \text{ to } -4.5] \, \text{m s}^{-1}$ at W band corresponds to about $[-4 \text{ to } -7.5] \, \text{m s}^{-1}$ at X band (see Fig. 5 in Tian et al. 2007). X-band Doppler velocities are similar to pure Rayleigh Doppler velocities for rain rates less than about $20 \, \text{mm h}^{-1}$. Rayleigh velocities of $[-4 \text{ to } -7.5] \, \text{m s}^{-1}$ correspond to a gamma distribution of droplets with $[0.6 \text{ to } 1.5]$-mm mode diameter (Steiner et al. 2004), which is typical for light rain ($0.1–5 \, \text{mm h}^{-1}$). Thus, the observed mean W-band Doppler velocities are consistent with our NRCS rain-rate estimates.

d. Attenuation corrections of observed reflectivity

To compute (18) to correct the measured $\text{dB}Z_{\text{em}}$ for attenuation, we must integrate along the entire propagation path from the aircraft to the surface. However, the radar's first range gate is 0.5 km below the
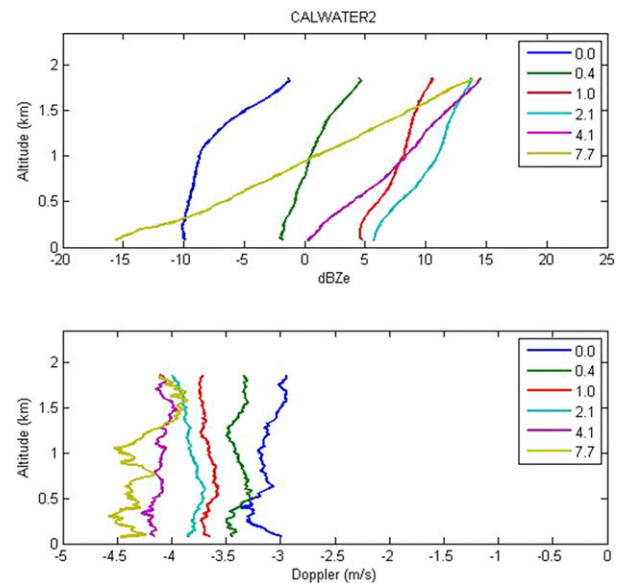
FIG. 7. Profiles of bin averages of (top) $\text{dB}Z_{\text{em}}$ and (bottom) pitch-corrected Doppler vertical velocity for 3 h on 5 Feb 2015. Legend gives the mean rain rate (mm h^{-1}) for the six rain-rate intervals of $[0–0.25, 0.25–0.7, 0.7–1.5, 1.5–3, 3–6, \text{ and } 6–13] \, \text{mm h}^{-1}$. Means were computed for profiles where SNR exceeded the threshold ($-10 \, \text{dB}$) for valid Doppler velocity estimates.

TABLE 4. Summary statistics of rain-rate-average reflectivity properties: f_q is the fraction of valid returns in each rain-rate category; $Z_{em}(0.1)$ is the return-fraction weighted mean measured reflectivity at 0.1-km altitude, Z_{ei} is the weighted measured profile extrapolated to the aircraft altitude; $Z_e(0.1)$ and Z_e (*top*) are retrieved reflectivity at 0.1-km altitude and aircraft height, respectively. The $10^{-\beta*\mathrm{PIA}/10}$ is the first term in the denominator of (20), and $q*S(h_s)$ is the second term evaluated at aircraft altitude ($h = 0$). Term $\Delta \mathrm{dB}Z_{et}$ is the total correction made via (20) to the reflectivity at aircraft altitude. The last two columns show the result using the direct γ–Z_e fits from the P-3 PIP and Matrosov (2010), respectively, given in Table 2.

$<R>$		PIA	$Z_{em}(0.1)$	Z_{ei}	$Z_e(0.1)$	$Z_e(top)$			$\Delta \mathrm{dB}Z_{et}$	$\Delta \mathrm{dB}Z_{et}$	$\Delta \mathrm{dB}Z_{et}$
mm h^{-1}	f_q	dB	dBZ	dBZ	dBZ	dBZ	$10^{-\beta*\mathrm{PIA}/10}$	$q*S(h_s)$	Bootstrap	P-3 PIP	Matrosov
0	0.29	0.3	−19.0	−0.2	−18.8	−0.5	0.93	0.029	0.2	0.2	0.25
0.4	0.42	2.0	−9.1	3.0	−7.5	4.4	0.63	0.10	1.3	1.7	1.6
1.0	0.59	4.4	−1.8	7.5	0.9	8.9	0.36	0.35	1.4	2.6	2.4
2.1	0.94	8.9	5.8	14.3	12.0	14.4	0.13	0.84	0.1	2.0	2.1
4.1	0.97	16.8	1.2	18.5	13.7	18.3	2.1E-2	1.01	−0.1	2.6	2.2
7.7	1.00	31.8	−13.6	21.7	15.6	21.6	6.6E-4	1.00	0	3.5	2.5

aircraft. Thus, we need to fill in the dBZ_{em} profile from the aircraft out to the first range gate. We have done this by fitting a linear regression to the mean dBZ_{em} profile starting at 1.83-km altitude and ending at 1.33-km altitude. Then, using the slope and intercept of the fit to the profile, we extrapolate dBZ_{em} values in 19 additional range gates between range gate 1 and the aircraft altitude. This is a total of 169 range gates going from the surface to the aircraft altitude. This is illustrated in Fig. 8, where mean dBZ_{em} are shown for the six selected rain-rate intervals used in Fig. 7. The extrapolated portions of the profiles are shown as dotted symbols. In Fig. 8 (and subsequent figures) the measured reflectivity dBZ_{em} is weighted by f_q to represent the average measured reflectivity within the rain-rate interval (not just the reflectivity while it is raining). The weight form is calculated by multiplying Z_{em} by f_q.

We have used the average measured unweighted reflectivity profiles as inputs into (20) and then the retrieved values are multiplied by f_q to yield "true" weighted dBZ_e profiles, which are shown as dashed lines in Fig. 8. We experimented with different parameters in the γ–Z_e relationship given in (16) but settled on $\alpha_\gamma = 0.050$ and $\beta_\gamma = 1.0$ based on the reflectivity intercept values. The near-surface part of the corrected reflectivity profile is not sensitive to the coefficients because it is set by PIA. The relative effects of PIA versus the γ–Z_e relationship can be gauged by noting the two terms in the denominator of (20). At the surface the $q[S(h_s) - S(h)]$ term is zero, yielding

$$\mathrm{dB}Z_{e0} = \mathrm{dB}Z_{em0} + \mathrm{PIA}. \qquad (24)$$

The sensitivity to PIA disappears at heights where $q[S(h_s) - S(h)] \gg 10^{-\beta*\mathrm{PIA}/10}$.

One measure of the profile retrieval's effectiveness can be evaluated at the top of the profile ($h = 0$), where

we expect the retrieved values to be the same as the observed (unattenuated) values. Thus, we expect the correction at $h = 0$ to be small,

$$\Delta \mathrm{dB}Z_{et} = -\frac{10}{\beta}\log_{10}\{[10^{-\beta*\mathrm{PIA}/10} + qS(h_s)]\} = 0. \qquad (25)$$

Values for $10^{-\beta*\mathrm{PIA}/10}$, $qS(h_s)$, and $\Delta \mathrm{dB}Z_{et}$ are given in Table 4 using $\alpha_\gamma = 0.050$ and $\beta_\gamma = 1.0$. Also, values of $\Delta \mathrm{dB}Z_{et}$ derived from the direct fit from the P-3 PIP ($\alpha_\gamma = 058, \beta_\gamma = 0.85$) and Matrosov ($\alpha_\gamma = 0.033, \beta_\gamma = 0.97$) are given in Table 4. The bootstrap values yield negligible corrections for the heavier rain rates, while the PIP and Matrosov values yield corrections on the order of 2–3 dB.

Two things to notice from Fig. 8 are that the corrected profiles are not perfectly vertically homogeneous. The profile for the lowest rain-rate bin, for which the
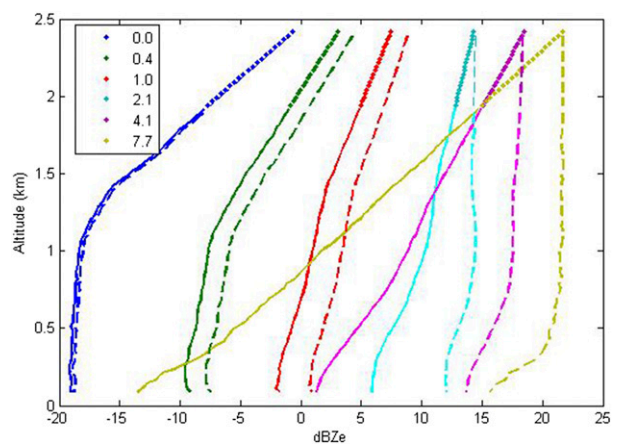
FIG. 8. Profiles of average dBZ_{em} and mean dBZ_e for the same rain-rate intervals used in Fig. 7. Average measured reflectivities are from Fig. 7a but have been scaled by f_q (see Table 4). Average dBZ_{em} (solid lines). Portions of the profiles above 1.9 km that are the extrapolations using the slope and intercepts (dotted lines). The term dBZ_e was computed from dBZ_{em} using (20) with $\gamma_R = 0.05*Z_{em}^{1.0}$

correction has no effect, is the most inhomogeneous. At rain rates of $1.0\,\mathrm{mm\,h^{-1}}$ and above the profiles are reasonably vertically homogeneous, except at the highest rain rate below 0.5-km altitude. The second thing to notice is that the Z_e values are quite close to the values (Z_{ei}) extrapolated to the height of the aircraft from the measured profiles. This suggests the consistency between precipitation retrievals and values of the reflectivity, the γ–Z_e relationship, and NRCS. The differences in the extrapolated reflectivities and the measured values at 500 m below the aircraft are consistent with the results shown in Figs. 1 and 2 of Hogan et al. (2003). Figure 1 in Hogan et al. shows estimates of unattenuated reflectivities as a function of rain rate; their Fig. 2b shows estimates of reflectivity after attenuation through 500 m at these same rain rates. The differences increase from 2 to 7 dB as the rain rate increases from 1 to $8\,\mathrm{mm\,h^{-1}}$. For the same rain rates, the differences values at 500 m below the aircraft with extrapolated values in Fig. 8 increase from 2 to 8 dB.

e. Evaluation of Z_e–R, γ–R, and γ–Z_e relationships at W band

It is well known that, because of the complexity and variability of rain microphysics, there are no universal Z_e–R, γ–R, and γ–Z_e relationships. Table 2 gives examples of variability for the W band. To determine relationships for a given set of observations Z_e–R and γ–Z_e relationships requires unattenuated Z_e values, which is problematical at W band, where attenuation is substantial. We have two sources of unattenuated Z_e: estimates at the aircraft altitude obtained by extrapolating the profiles of $\mathrm{dB}Z_{em}$ (the intercept occurs at $h = 0$, so it is unaffected by attenuation) and estimates of $\mathrm{dB}Z_e$ obtained by applying (20) to the observed profiles. This retrieval requires an assumed γ–Z_e relationship. We used the $\mathrm{dB}Z_e$ intercepts to determine the Z_e–R, γ–R, and γ–Z_e parameters and then verified that the retrieved Z_e were reasonably well fit.

Figure 9 shows the mean Z_e values (upper panel) and the mean attenuation (lower panel) at three altitudes as a function of the bin-average rain rate. We selected three levels from the retrieval plus the intercept because that is at most as many degrees of freedom in the profiles. We did not use near-surface profiles because of the anomalous behavior of the highest rain-rate profile below 0.5-km altitude. In the case of reflectivity, the value extrapolated from the uncorrected reflectivity (Z_{ei}) is shown as the square. In Fig. 10 we show the γ_R values from Fig. 9b plotted against the Z_e values from Fig. 9a. In Fig. 10 we can see residual attenuation (on the order of $1\,\mathrm{dB\,km^{-1}}$) as Z_e approaches 0. The γ–Z_e parameters used in the correction are shown to be a good fit to the data. The fits shown in these graphs are given as the bootstrap values in Table 2.
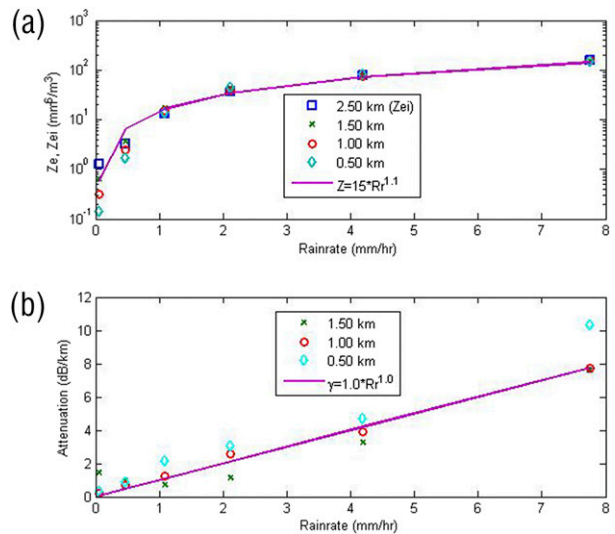
FIG. 9. Results from analysis of each mean profile using retrieved values of Z_e (Fig. 8) and extrapolations of linear regression fits of the form $\mathrm{dB}Z_{em} = \mathrm{dB}Z_{ei} + \mathrm{slope}*h$. (a) W-band $\mathrm{dB}Z_{em}$ extrapolated to the aircraft altitude as a function of NRCS rain rate (square) and retrieved values of unattenuated Z_e at heights of 0.5, 1.0, and 1.5 km vs rain rate. (b) One-way attenuation coefficient ($\mathrm{dB\,km^{-1}}$) vs rain rate. Points plotted are mean $\mathrm{dB}Z_e$ and attenuation at heights of 0.5, 1.0, and 1.5 km.

f. Profiles of rain rate

Finally, we present the mean rain-rate profiles obtained by averaging the profile of the vertical derivative of $\mathrm{dB}Z_{em}$ in rain-rate bins. While individual 0.3-s $\mathrm{dB}Z_{em}$ profiles yield a noisy derivative profile, when averaged the results are reasonably smooth. We then use (9) and (11) to compute the profiles of the rain rate (Fig. 11a) with $R = 1.15*\gamma$ as discussed in section 3b. If we had used the bootstrap parameters, then R would be 15% lower. We have multiplied the rain rate by the fraction of bins with detectable rain to yield an actual rain rate including the dry periods. Figure 11b shows rain-rate profiles retrieved via the R–Z_e relationship [(7)] with the corrected reflectivities—a clear illustration of why the hybrid method works. The bias in the attenuation-derived rain rates is apparent compared to the R–Z_e-derived values, particularly at low rain rates. Using the bootstrap parameters improves the agreement for higher rain rates.

g. Summary rain-rate statistics

In Table 3 we compare simple statistics for the different rain-rate estimates. We have added one estimate that is independent of the W-band radar, Rain2—the mean of the WSRA and SFMR rain rates. Rain2 has the same mean rain rate as rain from NRCS. The grand mean rain rate across all methods is $1.12 \pm 0.17\,\mathrm{mm\,h^{-1}}$;
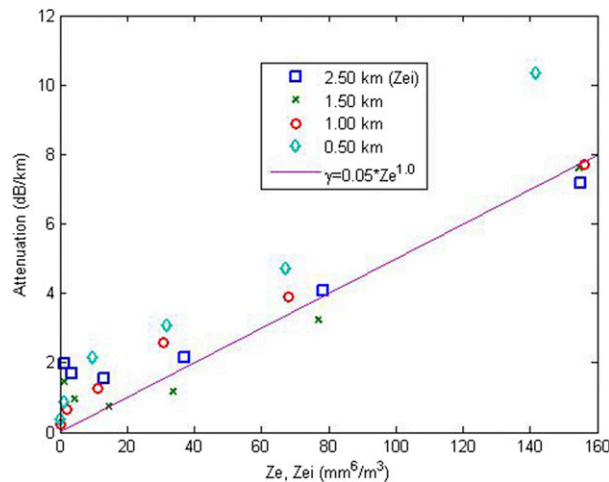
FIG. 10. Results from analysis of profiles as per Fig. 9, except that attenuation is plotted directly against Z_e.

the mean while raining is $2.18 \pm 0.21 \, \mathrm{mm \, h^{-1}}$. The hybrid method and SFMR have the highest correlations with R_{nc}. Note that the hybrid method, which depends on the observed reflectivity at 0.5 and 2.0 km below the aircraft and on the Doppler return at 0.5 km below the aircraft, is independent of R_{nc}, which depends on the reflectivity of the ocean surface.

5. Discussion and conclusions

In this paper we examined several approaches to estimating rain-rate time series, profiles, and statistics using radar reflectivity. The data are from the PSD W-band Doppler radar deployed on a NOAA P-3 aircraft during the CalWater-2 field program. Our primary goal was to investigate the use of the radar signal attenuation to improve estimates of rain rate and precipitation microphysical parameters below the aircraft (observation altitude was 2.5 km). The analysis is limited to 3 h from a flight in wide-scale frontal precipitation on 5 February 2015. In principle, profiles of rain rate can be computed from the profile of attenuation if cloud absorption and vertical inhomogeneity are negligible. However, individual profiles (3-Hz acquisition rate) may be quite vertically inhomogeneous because of the patchy nature of precipitation—this leads to noisy vertical derivatives. We used 1-min averages to smooth out some of the inhomogeneity.

The relationship of attenuation coefficient to the rain rate was found to be near linear and quite robust with good comparisons of our observations with several others in the literature. At rain rates near $1 \, \mathrm{mm \, h^{-1}}$ and below, the observed attenuation coefficient levels off, which is a possible consequence of cloud attenuation.
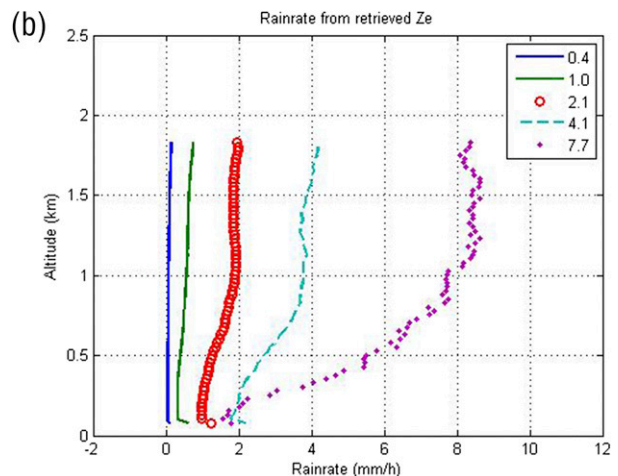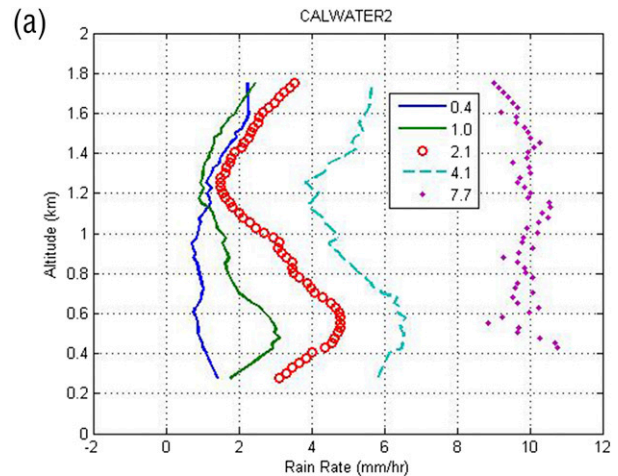
FIG. 11. Rain-rate bin-averaged profiles of rain rate from the (a) averaged $\mathrm{dB}Z_{em}$ slope and (b) retrieved Z_e values (Fig. 8) using the bootstrap Z–R relationship in Table 2.

The relationships of reflectivity factor with rain rate or attenuation coefficient were also robust. Our W-band radar measurements, after correction for attenuation, were a good fit to an assumed power law of $\gamma = \alpha_\gamma Z_e^{\beta_\gamma}$ (Fig. 10) and compared reasonably with fits to computations using measured DSDs (see Table 2).

The NRCS method provided the most consistent estimate of layer-averaged rain rate from the W band, though, unlike the reflectivity gradient methods, it is applicable when the surface backscatter in the absence of rain is well characterized. Uncertainty in the rain–attenuation relationship makes the rain-rate values uncertain by about 15%. Uncertainty in the water vapor or cloud attenuation and in the NRCS wind speed parameterization contributes an additional rain-rate uncertainty of about $\pm 0.5 \, \mathrm{mm \, h^{-1}}$. Without a standard we are unable to discern which of the rain estimates is

superior. The most obvious difference between NRCS, WSRA, and SFMR-based methods is in the behavior in lighter rainfall. The SMFR tends to be spikey with very little light rain, while the WSRA shows higher values in light rain. The WSRA-based estimates are expected to be unbiased, but because of weaker attenuation they are also expected to have more trouble resolving light rain. The three other methods (i.e., methods 1–3) for estimating rainfall from W-band dBZ_{em} profiles/gradients were not as effective as the NRCS method. The two gradient methods were unreliable in inhomogeneous rain distributions when rain is not present at all altitudes below the aircraft. The hybrid method of Chandra et al. (2015), which combines an R–Z_{em} retrieval in light rain and an R–γ gradient-based retrieval in heavier rain was better with a 0.79 correlation with R_{nc}.

Compositing dBZ_{em}, Doppler velocity, or $\partial dBZ_{em}/\partial z$ in bins of rain rate (Figs. 7, 8, and 11) yields very clean profiles. At lower rain rates there are anomalous gradients of dBZ_e in the upper heights, presumably because light rain is occurring at higher altitudes but is not reaching the surface. The profiles of mean gradient-derived rain rate in bins of NRCS rain rate (Fig. 11a) are smooth and the values are consistent at higher rain rates (but about 10% higher than NRCS-based rain-rate estimates). The use of the NRCS-referenced Iguchi and Meneghini (1994) method to reconstruct unattenuated profiles of dBZ_e from the composited observed (attenuated values) was robust. The retrieved profiles were consistent with estimates of unattenuated reflectivity from linear regressions of Z_{em} against range. The observed relationship of the corrected reflectivity with measured attenuation was consistent with the relationship assumed in the retrieval.

For research in cloud physics and cloud turbulence from mobile platforms (aircraft or ships), a W-band Doppler radar is likely the optimal choice. The combination of small size, sensitivity, narrow beamwidth, and reasonable (relatively) cost make it feasible to find installation space on crowded research aircraft and to stabilize pitch and roll motions on ships. For airborne systems a narrow beamwidth is necessary to minimize the broadening of the Doppler width ($0.45\,\mathrm{m\,s^{-1}}$ broadening for the NOAA W band on the P-3 aircraft). For the measurement of rain rate with a single radar, a longer wavelength radar with less attenuation is likely preferable—depending on the scientific target. However, for space, weight, and sensitivity reasons, the W band might be preferred for ice cloud/precipitation studies from a high-altitude aircraft, such as the NCAR High-Performance Instrumented Airborne Platform for Environmental Research (HIAPER; (Vivekanandan et al. 2015). Clearly multiple wavelength approaches are

preferable, but there are engineering challenges. Installing a Ku-band system with the same beamwidth ($0.7°$) as the NOAA W band would mean finding a place for a 1.5-m-diameter antenna.

REFERENCES

Black, P. G., and C. T. Swift, 1984: Airborne stepped frequency microwave radiometer measurements of rainfall rate and surface wind speed in hurricanes. Preprints, *Second Conf. on Radar Meteorology*, Zurich, Switzerland, Amer. Meteor. Soc., 433–438.

Chandra, A., C. Zhang, P. Kollias, S. Matrosov, and W. Szyremr, 2015: Automated rain rate estimates using the Ka-band ARM zenith radar (KAZR). *Atmos. Meas. Tech.*, **8**, 3685–3699, https://doi.org/10.5194/amt-8-3685-2015.

Ciach, G., 2003: Local random errors in tipping-bucket rain gauge measurements. *J. Atmos. Oceanic Technol.*, **20**, 752–759, https://doi.org/10.1175/1520-0426(2003)20<752:LREITB>2.0.CO;2.

Fairall, C. W., S. Pezoa, K. Moran, and D. Wolfe, 2014: An observation of sea-spray microphysics by airborne Doppler radar. *Geophys. Res. Lett.*, **41**, 3658–3665, https://doi.org/10.1002/2014GL060062.

Foote, G. B., and P. A. duToit, 1969: Terminal velocity of raindrops aloft. *J. Appl. Meteor.*, **8**, 249–253, https://doi.org/10.1175/1520-0450(1969)008<0249:TVORA>2.0.CO;2.

Firda, J. M., S. M. Sekelsky, and R. E. McIntosh, 1999: Application of dual-frequency millimeter-wave Doppler spectra for the retrieval of drop size distributions and vertical air motion in rain. *J. Atmos. Oceanic Technol.*, **16**, 216–236, https://doi.org/10.1175/1520-0426(1999)016<0216:AODFMW>2.0.CO;2.

Frisch, A. S., C. W. Fairall, and J. B. Snider, 1995: Measurement of stratus cloud and drizzle parameters in ASTEX with a K_α-band Doppler radar and a microwave radiometer. *J. Atmos. Sci.*, **52**, 2788–2799, https://doi.org/10.1175/1520-0469(1995)052<2788:MOSCAD>2.0.CO;2.

——, G. Feingold, C. W. Fairall, T. Uttal, and J. B. Snider, 1998: On cloud radar and microwave radiometer measurements of stratus cloud liquid water profiles. *J. Geophys. Res.*, **103**, 23 195–23 197, https://doi.org/10.1029/98JD01827.

Galloway, J., and Coauthors, 1999: Coincident in situ and W-Band radar measurements of drop size distribution in a marine stratus cloud and drizzle. *J. Atmos. Oceanic Technol.*, **16**, 504–517, https://doi.org/10.1175/1520-0426(1999)016<0504:CISAWB>2.0.CO;2.

Ghate, V. P., B. A. Albrecht, M. A. Miller, A. Brewer, and C. W. Fairall, 2014: Turbulence and radiation in stratocumulus topped marine boundary layers: A case study from VOCALS-Rex. *J. Appl. Meteor. Climatol.*, **53**, 117–135, https://doi.org/10.1175/JAMC-D-12-0225.1.

Haimov, S., and A. Rodi, 2013: Fixed-antenna pointing-angle calibration of airborne Doppler cloud radar. *J. Atmos. Oceanic Technol.*, **30**, 2320–2335, https://doi.org/10.1175/JTECH-D-12-00262.1.

Haynes, J. M., T. S. L'Ecuyer, G. L. Stephens, S. D. Miller, C. Mitrescu, N. B. Wood, and S. Tanelli, 2009: Rainfall retrieval over the ocean with spaceborne W-band radar. *J. Geophys. Res.*, **114**, D00A22, https://doi.org/10.1029/2008JD009973.

Heymsfield, G. M., 1989: Accuracy of vertical air motions from nadir-viewing Doppler airborne radars. *J. Atmos. Oceanic Technol.*, **6**, 1079–1082, https://doi.org/10.1175/1520-0426(1989)006<1079:AOVAMF>2.0.CO;2.

Hitschfeld, W., and J. Bordan, 1954: Errors inherent in the radar measurement of rainfall at attenuating wavelengths. *J. Meteor.*, **11**, 58–67, https://doi.org/10.1175/1520-0469(1954)011<0058:EIITRM>2.0.CO;2.

Hogan, R. J., D. Bouniol, D. N. Ladd, E. J. O'Connor, and A. J. Illingworth, 2003: Absolute calibration of 94/95-GHz radars using rain. *J. Atmos. Oceanic Technol.*, **20**, 572–580, https://doi.org/10.1175/1520-0426(2003)20<572:ACOGRU>2.0.CO;2.

Iguchi, T., and R. Meneghini, 1994: Intercomparison of single-frequency methods for retrieving a vertical rain profile from airborne or spaceborne radar data. *J. Atmos. Oceanic Technol.*, **11**, 1507–1516, https://doi.org/10.1175/1520-0426(1994)011<1507:IOSFMF>2.0.CO;2.

Klotz, B. W., and E. W. Uhlhorn, 2014: Improved stepped frequency microwave radiometer tropical cyclone surface winds in heavy precipitation. *J. Atmos. Oceanic Technol.*, **31**, 2392–2408, https://doi.org/10.1175/JTECH-D-14-00028.1.

Kollias, P., B. A. Albrecht, and F. D. Marks Jr., 2003: Cloud radar observations of vertical drafts and microphysics in convective rain. *J. Geophys. Res.*, **108**, 4053, https://doi.org/10.1029/2001JD002033.

——, M. A. Miller, E. P. Luke, K. L. Johnson, E. E. Clothiaux, K. P. Moran, K. B. Widener, and B. A. Albrecht, 2007: The Atmospheric Radiation Measurement Program cloud profiling radars: Second-generation sampling strategies, processing, and cloud data products. *J. Atmos. Oceanic Technol.*, **24**, 1199–1214, https://doi.org/10.1175/JTECH2033.1.

Lakshmanan, V., T. Smith, K. Hondl, G. Stumpf, and A. Witt, 2006: A real-time, three-dimensional, rapidly updating, heterogeneous radar merger technique for reflectivity, velocity, and derived products. *Wea. Forecasting*, **21**, 802–823, https://doi.org/10.1175/WAF942.1.

Lee, G., and I. Zawadzki, 2006: Radar calibration by gage, disdrometer, and polarimetry: Theoretical limit caused by the variability of drop size distribution and application to fast scanning operational radar data. *J. Hydrol.*, **328**, 83–97, https://doi.org/10.1016/j.jhydrol.2005.11.046.

Lhermitte, R. M., 2002: *Centimeter and Millimeter Wavelength Radars in Meteorology.* Lhermitte Publications, 550 pp.

Li, L., G. M. Heymsfield, L. Tian, and P. E. Racette, 2005: Measurements of ocean surface backscattering using an airborne 94-GHz cloud radar—Implications for calibration of airborne and spaceborne W-band radars. *J. Atmos. Oceanic Technol.*, **22**, 1033–1045, https://doi.org/10.1175/JTECH1722.1.

Matrosov, S. Y., 2007: Potential for attenuation-based estimations of rainfall from CloudSat. *Geophys. Res. Lett.*, **34**, L05817, https://doi.org/10.1029/2006GL029161.

——, 2009: A method to estimate vertically integrated amounts of cloud ice and liquid and mean rain rate in stratiform precipitation from radar and auxiliary data. *J. Appl. Meteor. Climatol.*, **48**, 1398–1410, https://doi.org/10.1175/2009JAMC2106.1.

——, 2010: Evaluating polarimetric X-band radar rainfall estimators during HMT. *J. Atmos. Oceanic Technol.*, **27**, 122–134, https://doi.org/10.1175/2009JTECHA1318.1.

——, 2011: CloudSat measurements of landfalling hurricanes Gustav and Ike (2008). *J. Geophys. Res.*, **116**, D01203, https://doi.org/10.1029/2010JD014506.

Meneghini, R., J. Eckerman, and D. Atlas, 1983: Determination of rain rate from a spaceborne radar using measurements of total attenuation. *IEEE Trans. Geosci. Remote Sens.*, **GE-21**, 34–43, https://doi.org/10.1109/TGRS.1983.350528.

Moran, K., S. Pezoa, C. W. Fairall, C. Williams, T. Ayers, A. Brewer, S. P. de Szoeke, and V. Ghate, 2012: A motion-stabilized W-band radar for shipboard observations of marine boundary-layer cloud. *Bound.-Layer Meteor.*, **143**, 3–24, https://doi.org/10.1007/s10546-011-9674-5.

Ralph, F. M., and Coauthors, 2016: CalWater field studies designed to quantify the roles of atmospheric rivers and aerosols in modulating U.S. West Coast precipitation in a changing climate. *Bull. Amer. Meteor. Soc.*, **97**, 1209–1228, https://doi.org/10.1175/BAMS-D-14-00043.1.

Steiner, M., J. A. Smith, and R. Uijlenhoet, 2004: A microphysical interpretation of radar reflectivity–rain rate relationships. *J. Atmos. Sci.*, **61**, 1114–1131, https://doi.org/10.1175/1520-0469(2004)061<1114:AMIORR>2.0.CO;2.

Tian, L., G. M. Heymsfield, L. Li, and R. C. Srivastava, 2007: Properties of light stratiform rain derived from 10- and 94-GHz airborne Doppler radar measurements. *J. Geophys. Res.*, **112**, D11211, https://doi.org/10.1029/2006JD008144.

Tridon, F., and A. Battaglia, 2015: Dual-frequency radar Doppler spectra retrieval of rain drop size distributions and entangled dynamics variables. *J. Geophys. Res. Atmos.*, **120**, 5585–5601, https://doi.org/10.1002/2014JD023023.

——, ——, and P. Kollias, 2013: Disentangling Mie and attenuation effects in rain using a K_a-W dual-wavelength Doppler spectral ratio technique. *Geophys. Res. Lett.*, **40**, 5548–5552, https://doi.org/10.1002/2013GL057454.

Uhlhorn, E. W., P. G. Black, J. L. Franklin, M. Goodberlet, J. Carswell, and A. S. Goldstein, 2007: Hurricane surface wind measurements from an operational stepped frequency microwave radiometer. *Mon. Wea. Rev.*, **135**, 3070–3085, https://doi.org/10.1175/MWR3454.1.

Vivekanandan, J., and Coauthors, 2015: A wing pod-based millimeter wavelength airborne cloud radar. *Geosci. Instrum. Methods Data Syst.*, **4**, 161–176, https://doi.org/10.5194/gi-4-161-2015.

Walsh, E. J., I. PopStefanija, S. Y. Matrosov, J. Zhang, E. Uhlhorn, and B. Klotz, 2014: Airborne rain-rate measurement with a Wide-Swath Radar Altimeter. *J. Atmos. Oceanic Technol.*, **31**, 860–875, https://doi.org/10.1175/JTECH-D-13-00111.1.

Williams, C. R., 2012: Vertical air motion retrieved from dual-frequency profiler observations. *J. Atmos. Oceanic Technol.*, **29**, 1471–1480, https://doi.org/10.1175/JTECH-D-11-00176.1.

——, 2016: Reflectivity and liquid water content vertical decomposition diagrams to diagnose vertical evolution of raindrop size distributions. *J. Atmos. Oceanic Technol.*, **33**, 579–595, https://doi.org/10.1175/JTECH-D-15-0208.1.

Zhang, J., and Coauthors, 2011: National Mosaic and Multi-Sensor QPE (NMQ) system: Description, results, and future plans. *Bull. Amer. Meteor. Soc.*, **92**, 1321–1338, https://doi.org/10.1175/2011BAMS-D-11-00047.1.